## Quantum sensing of local stray field environment of micron-scale magnetic disks

Jingcheng Zhou<sup>1</sup>, Gerald Q. Yan<sup>1</sup>, Mengqi Huang<sup>1</sup>, Nathan J. McLaughlin<sup>1</sup>, Chunhui Rita Du<sup>1,2</sup>, Hailong Wang<sup>2,\*</sup>

<sup>1</sup>Department of Physics, University of California, San Diego, La Jolla, California 92093, USA <sup>2</sup>Center for Memory and Recording Research, University of California, San Diego, La Jolla, California 92093-0401, USA

\*Corresponding author: <u>h3wang@physics.ucsd.edu</u>

Abstract: Local characterization of the properties and performances of miniaturized magnetic devices is a prerequisite for advancing present on-chip spintronic technologies. Utilizing nitrogenvacancy (NV) centers in diamond, here we report quantum sensing of spin wave modes and magnetic stray field environment of patterned micron-scale Y<sub>3</sub>Fe<sub>5</sub>O<sub>12</sub> (YIG) disks at the submicron length scale. Taking advantage of wide-field magnetometry techniques using NV ensembles, we map the spatially dependent NV electron spin resonances and Rabi oscillations in response to local variations of the stray fields emanating from a proximal YIG pattern. Our experimental data are in excellent agreement with theoretical predictions and micromagnetic simulation results, highlighting the significant opportunities offered by NV centers for probing the local magnetic properties of functional solid-state devices. The presented quantum sensing strategy may also find applications in the development of next-generation spintronic circuits with improved scalability and density.

Patterned magnetic microstructures with desirable magneto-transport and optical properties are used as building blocks for modern spintronic technologies. Over the past decades, a range of magnetic devices featuring on-demand functionalities such as tunneling magnetoresistance, 2-4 magnetoresistive random-access memory, 5,6 and spin-orbit-torque driven magnetic switching<sup>7,8</sup> have been intensively explored in this context. As the miniaturization of these on-chip spintronic circuits continues, experimental tools capable of evaluating the local device properties in a more precise way are urgently required. Existing characterization methods mainly focus on diagnosing the electrical and magneto-transport performances of spintronic units.<sup>3-8</sup> At the present technological levels, the available experimental approaches capable of measuring the magnitude and spatial profile of local stray fields arising from individual micromagnetic units, which determines the dipole crosstalk and the ultimate device density, are still sparse. Nitrogen-vacancy (NV) center-based quantum metrology features competitive field sensitivity and high spatial resolution and is ideally posed to tackle these challenges. Many of the advantages behind this sensing technique result from the excellent quantum coherence, single-spin sensitivity, and remarkable functionality of NV centers under a broad range of experimental conditions.9-11 Using NV-based quantum magnetometry techniques, here we report wide field quantum sensing of micron-scale Y<sub>3</sub>Fe<sub>5</sub>O<sub>12</sub> (YIG) disks and local measurements of the resonant spin wave modes. 12-15 Our results are in excellent agreement with the theoretical predictions, highlighting the significant opportunities of NV centers for probing local magnetic properties of functional on-chip spintronic devices.

We first present the pertinent NV physics and our measurement platform as illustrated in Fig. 1(a). An NV center consists of a nitrogen atom adjacent to a carbon atom vacancy in one of the nearest neighboring sites of a diamond crystal lattice.  $^{9,16}$  It contains an S=1 electron spin with optically addressable, spin-dependent photoluminescence (PL) to perform cutting-edge magnetometry measurements. 9,16 In comparison with conventional magneto-optic techniques such as Brillouin light scattering, which mainly utilizes magnon-photon interactions to study magnon density in magnetic samples/devices, NV centers take full advantage of their intrinsic quantummechanical nature to quantitatively measure the magnetic field in a broad frequency bandwidth. 9,10,17,18 To date, NV magnetometry has been applied to investigate the local magnetic features of a variety of "hard" and "soft" material systems such as living cells, 19 correlated condensed matter materials, 12-15,20,21 dark matter, 22 and others. 9 In the current work, we utilized both NV confocal and wide-field microscopy to probe the spin wave excitations and stray field environment of YIG patterns. An optical image shown in Fig. 1(b) provides an overview of a prepared hybrid device for our NV measurements. Micron-scale YIG disks were fabricated by standard photolithography and dry etching methods from commercially available 100-nm-thick YIG films grown on a Gd<sub>3</sub>Ga<sub>5</sub>O<sub>12</sub> substrate. A (001) oriented diamond microchip<sup>23</sup> with lateral dimensions of 20  $\mu$ m  $\times$  20  $\mu$ m was placed on top of the YIG disk. NV centers were implanted on the bottom surface of the diamond chip with an estimated density of ~1500/µm<sup>2</sup>. An on-chip Au stripline was patterned next to the YIG disk for the purpose of delivering microwave currents to control the NV spin states and to excite spin wave modes in the YIG. The diamond microchip used in the current study contains four possible NV spin orientations (NV<sub>1</sub>, NV<sub>2</sub>, NV<sub>3</sub>, and NV<sub>4</sub>) along the characteristic vectorial directions of a diamond crystal lattice, whose in-plane projections on the sample surface are perpendicular to each other as shown in Fig. 1(c). We employed NV relaxometry methods to quantitatively characterize the distance between the NV centers and the top surface of the YIG pattern. 11,21,24-26 Magnetic noise at the NV electron spin resonance (ESR) frequencies generated by fluctuation of the transverse YIG spin density will induce NV spin transitions between the  $m_s = 0$  and  $m_s = \pm 1$  states [Fig. 1(d)]. Variation of the corresponding NV spin relaxation rates  $\Gamma_{\pm}$  ( $m_s = 0 \leftrightarrow \pm 1$ ) as a function of an external magnetic field  $B_{ext}$  aligned with one of the NV spin orientations sensitively depends on the intrinsic material parameters of

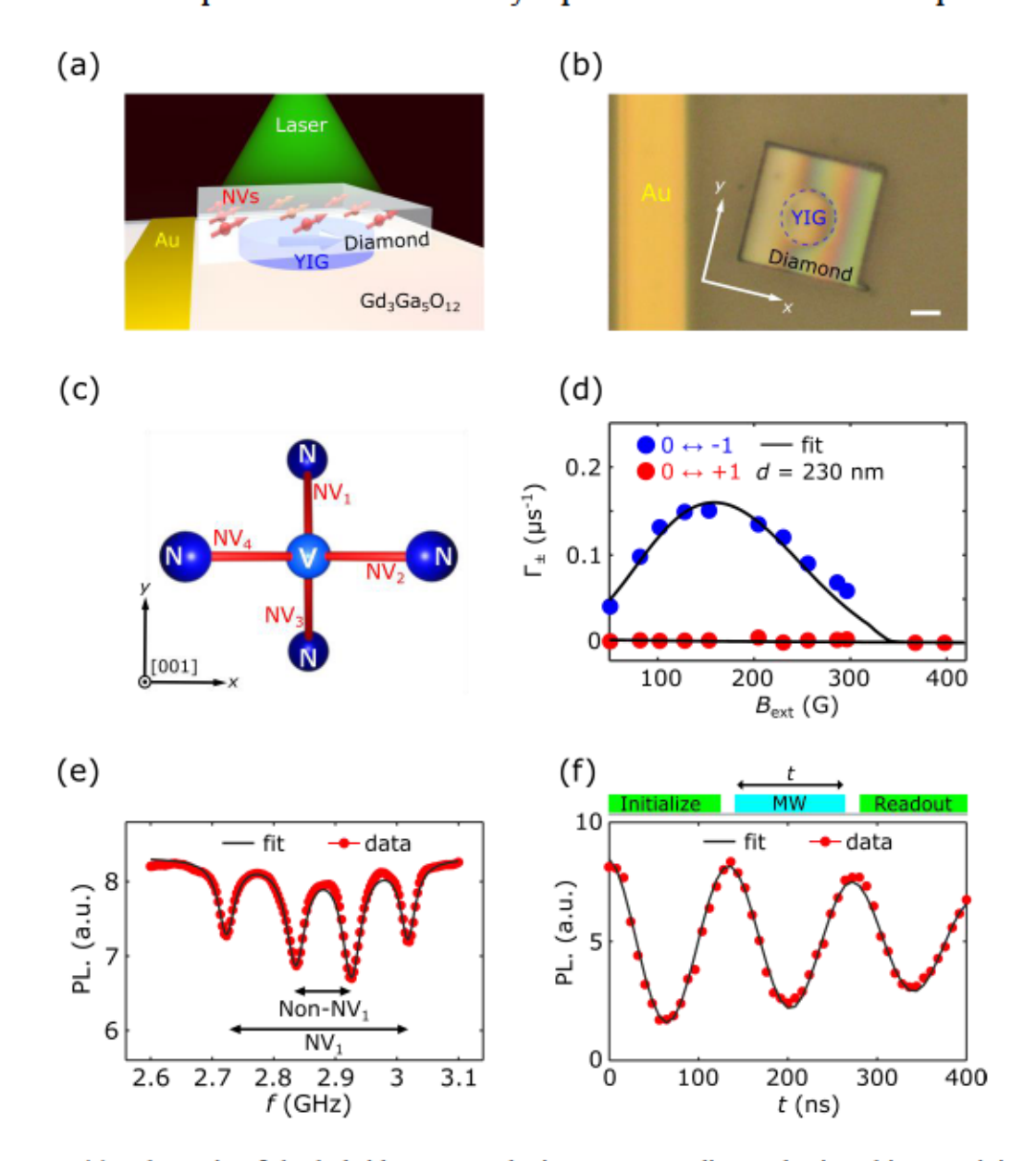


Figure 1. (a) Schematic of the hybrid NV-YIG device system: a diamond microchip containing NV ensembles is positioned on top of a patterned YIG microdisk. An on-chip Au stripline is used to deliver microwave currents to control NV spin states and to excite spin waves in the YIG pattern. (b) An optical microscope image showing an overview of a prepared device. The scale bar is 5  $\mu$ m. (c) Illustration of the in-plane projection of the four possible NV spin orientations on the (001) diamond sample surface. (d) NV spin relaxation rates  $\Gamma_{\pm}$  measured as a function of an external magnetic field  $B_{\text{ext}}$ . (e) ODMR spectrum of NV centers contained in the [001] oriented diamond with an external field  $B_{\text{ext}}$  applied along NV<sub>1</sub> spin axis direction. (f) Top panel: optical and microwave measurement sequence of NV Rabi oscillation measurements. Bottom panel: NV PL intensity measured as a function of the microwave pulse duration time t.

the prepared hybrid device. <sup>11</sup> Invoking a theoretical model developed in Ref. 11, the vertical NV-to-sample distance is estimated to be  $230 \pm 15$  nm. Such nanoscale proximity between NV centers and the patterned magnetic structure ensures a high field sensitivity for NV quantum sensing measurements reported in this work.

We first utilize NV confocal microscopy to demonstrate local sensing of spin wave modes and static magnetic field environment of the YIG disk. D.C. magnetometry measurements utilize the Zeeman effect of NV centers. 9,11 The longitudinal component of the stray field along the NV axes will lift the two-fold degeneracy of NV spin energy levels, which can be optically detected by NV ESR measurements. 9,11 In the current work, we applied continuous green laser excitation and microwave signals to perform NV ESR studies. An external magnetic field  $B_{\text{ext}}$  generated by a cylindrical NdFeB permanent magnet is aligned along one of the four possible NV spin directions (NV<sub>1</sub>). Figure 1(e) presents a typical set of the measured ESR spectrum, which exhibits two pairs of split NV spin energy levels. The outer pair corresponds to the Zeeman splitting of NV centers with spin orientation (NV1) aligned with the external magnetic field Bext while the inner one is three-fold degenerate, corresponding to NV centers with spin axes along the other possible directions. The magnitude of the local static magnetic field  $B_{tot}$  longitudinal to the NV<sub>1</sub> spin direction can be extracted as follows:  $B_{\text{tot}} = \pi \Delta f_{\text{NV}_1} / \tilde{\gamma}$ , where  $\Delta f_{\text{NV}_1}$  characterizes the Zeeman splitting of the aligned NVs and  $\tilde{\gamma}$  is the gyromagnetic ratio. Subtracting the contribution from the external magnetic field Bext, magnetic stray fields exclusively arising from the patterned YIG disk can be quantitatively measured.

Known as a qubit-based magnetometer, NV centers also act as a sensitive probe of local microwave magnetic fields. When a microwave magnetic field with NV ESR frequencies  $f_{\pm}$  is applied at NV sites, NV spins will periodically oscillate between two different states on the Bloch sphere, which is typically referred to as Rabi oscillations.<sup>27</sup> Here  $f_{+}$  characterize the NV ESR frequencies corresponding to spin transitions between the  $m_s = 0$  and  $m_s = \pm 1$  states. The top panel of Fig. 1(f) shows the optical and microwave sequence for NV Rabi oscillation measurements. A green laser pulse was first applied to initialize the NV spin to the  $m_s = 0$  state. A microwave pulse at a frequency  $f_{-}$  was then applied to drive the  $m_s = 0 \leftrightarrow -1$  transition followed by a second green laser pulse to measure spin-dependent NV PL and to re-initialize NV spin states. The duration of the microwave pulses is systematically changed to monitor the variation of the NV PL. The bottom panel of Fig. 1(f) presents an NV Rabi oscillation spectrum measured at an ESR frequency  $f_{-}$  of 1.86 GHz.

Next, we use NV confocal microscopy to perform optically detected magnetic resonance (ODMR) measurements to probe spin wave modes harbored by the patterned YIG disk. Figures 2(a) and 2(b) show the normalized NV PL as a function of the applied microwave frequency f and external magnetic field  $B_{\rm ext}$  for YIG microdisks with a diameter of 10  $\mu$ m and 16  $\mu$ m, respectively. The presented ODMR maps were measured by addressing NV centers positioned right above the YIG disk. The two straight lines emerging at ~2.87 GHz result from the expected decrease in NV fluorescence when the microwave frequency f matches the NV ESR frequencies. <sup>9,11</sup> NV fluorescence is also reduced when f matches the resonant frequency  $f_{\rm SW}$  of magnetostatic surface spin wave modes f of the YIG pattern as shown by the curved dashed lines. Sets of spin wave modes emerge due to the finite size effect of the YIG microdisk. The discrete wavevector values are determined by f magnetic disk. f magnetic di

intrinsic material parameters such as the amplitude of the spin wave modes, Gilbert damping constant, NV-to-sample distance, NV quality, and others.

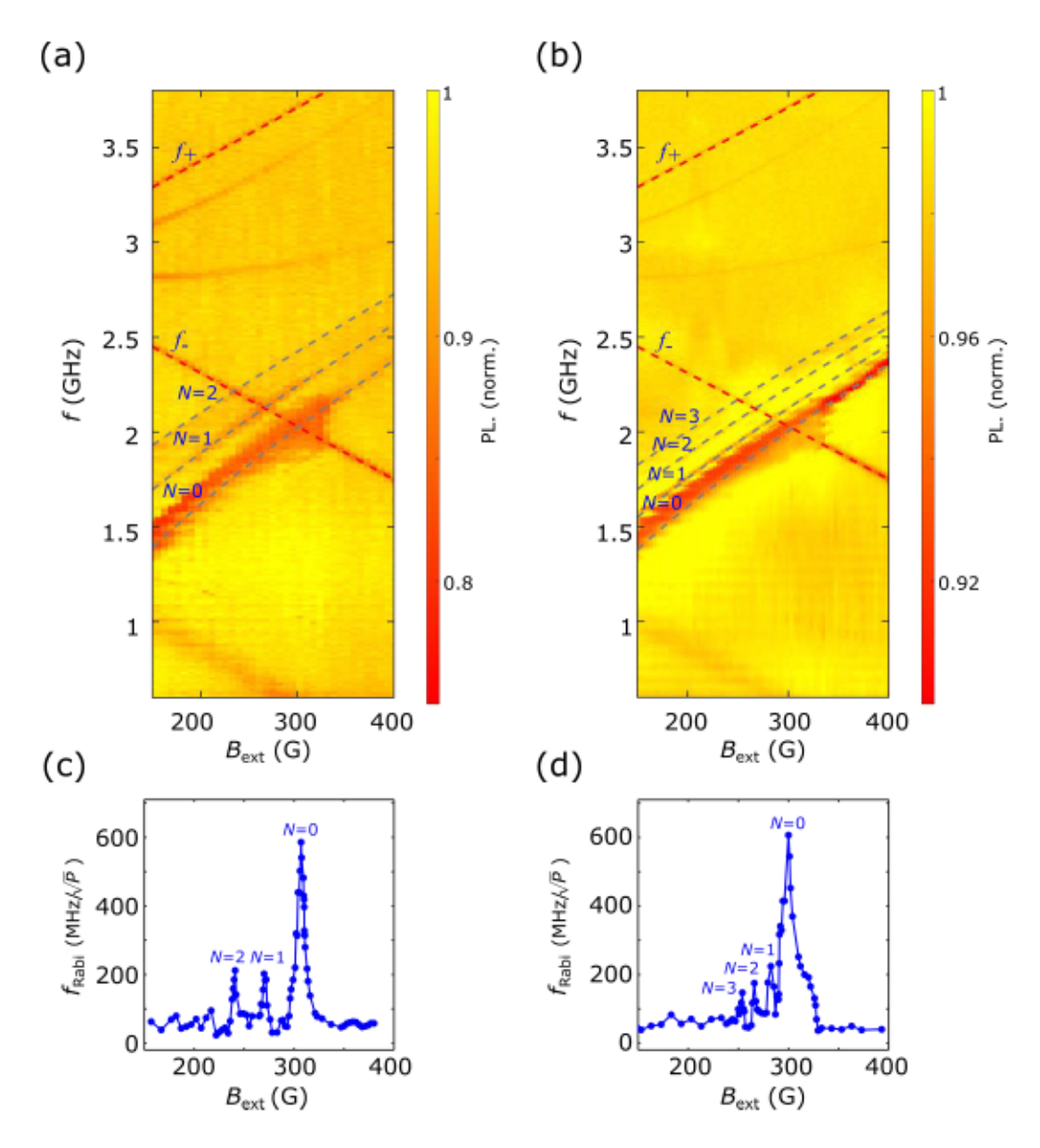


Figure 2. (a)-(b) Normalized NV PL as a function of the external magnetic field  $B_{\text{ext}}$  and microwave frequency f for a YIG microdisk with a diameter of 10  $\mu$ m (a) and 16  $\mu$ m (b), respectively. The straight dashed lines shown in the maps represent the NV ESR transitions, and the curved dashed lines represent the calculated dispersion curves of magnetostatic surface spin wave modes of the YIG microdisk with discrete wave vectors  $k_0$ ,  $k_1$ ,  $k_2$ , and  $k_3$ . (c)-(d) Normalized NV Rabi oscillation rate  $f_{\text{Rabi}}/\sqrt{P}$  as a function of the external magnetic field  $B_{\text{ext}}$  for the YIG microdisk with a diameter of 10  $\mu$ m (c) and 16  $\mu$ m (d), respectively. The input microwave frequency is set at the NV ESR frequency  $f_-$  in order to drive coherent spin rotation.

The spin wave modes excited in the YIG disks could enhance the amplitude of local microwave magnetic fields at proximal NV sites, leading to an increase in the NV Rabi oscillation

rate when  $f_{SW}$  matches the NV ESR frequency  $f_-$ . To illustrate this point, Figs. 2(c) and 2(d) present the normalized NV Rabi oscillation rate ( $f_{Rabi}/\sqrt{P}$ ) as a function of the external magnetic field  $B_{ext}$ . Note that the external microwave excitation frequency is fixed at  $f_-$  and the variation of the input microwave power P has been normalized to reflect the effective driving efficiency of NV spin rotation. One can see that  $f_{Rabi}/\sqrt{P}$  consistently shows peak values when  $f_-$  matches the resonant conditions of the  $k_0$ ,  $k_1$ ,  $k_2$ , and  $k_3$  magnetostatic surface spin wave modes. It is instructive to note that the enhancement ratio of  $f_{Rabi}/\sqrt{P}$  qualitatively decreases with the increasing wavevector number, which is attributed to the reduced microwave excitation efficiency of high order standing spin wave modes. 31

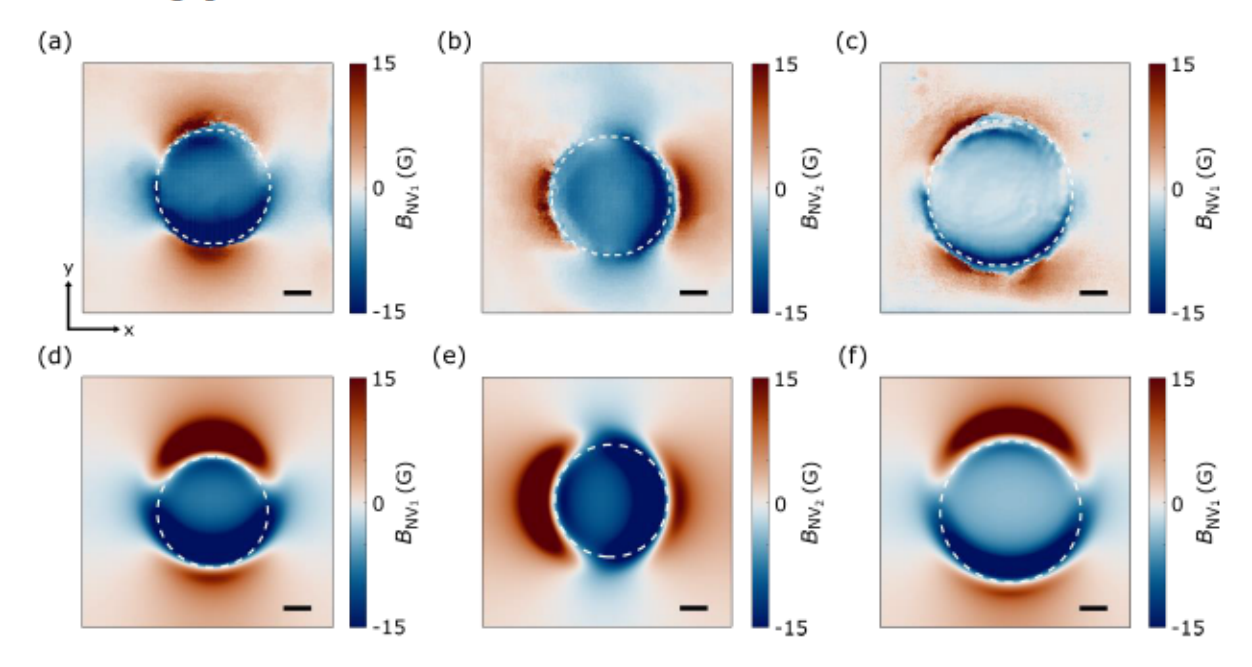


Figure 3. (a)-(b) 2D wide-field imaging of the longitudinal magnetic stray field  $B_{\rm NV_1}$  (a) and  $B_{\rm NV_2}$  (b) along the NV<sub>1</sub> and NV<sub>2</sub> spin directions, respectively. The diameter of the YIG disk of interest is 10 µm. (c) 2D wide-field imaging of the longitudinal magnetic stray field  $B_{\rm NV_1}$  arising from a larger YIG disk with a diameter of 16 µm. (d)-(f) Micromagnetic simulations of spatial distribution of the emanating magnetic stray field  $B_{\rm NV_1}$  ( $B_{\rm NV_2}$ ) corresponding to the experimental situations shown in (a)-(c). The white dashed lines outline the boundary of the YIG disk and scale bar is 2.5 µm.

We now utilize NV wide-field microscopy to probe the static magnetic stray field environment of the patterned YIG microdisk. The laser beam spot width used in our wide-field NV measurements is approximately  $\sim 26 \, \mu m \times 26 \, \mu m$ , allowing for simultaneous imaging of all the NV centers contained in the diamond microchip positioned on the YIG disk. The NV fluorescence is measured using a CMOS camera. We note that the ultimate spatial resolution of NV wide-field microscopy is determined by the optical diffraction limit, which is  $\sim 500 \, nm$  in the current study. 12,23 Figures 3(a) shows a 2D widefield image of the longitudinal component of the magnetic stray field  $B_{NV_1}$  along NV<sub>1</sub> spin axis, which is 54 degrees relative to the out-of-plane direction with an in-plane projection parallel to the y-axis. An external magnetic field  $B_{ext}$  of 400 G is applied along the selected NV spin direction during the wide-field measurements. Due to the strong in-plane anisotropy, the YIG magnetization remains in the disk plane and is uniformly aligned along the y-axis direction. It is evident that the magnetic stray field mainly emerges from

the two opposing sides of the YIG disk along the in-plane field direction, as is expected for a largely uniform magnetic distribution. Across each of these two edges, the emanating stray field reverses sign over the boundary of the pattern owing to its dipolar nature [Fig. 3(a)]. We also perform micromagnetic simulations of the stray field distribution of the YIG disk as shown in Fig. 3(d), which is in excellent agreement with our experimental results. When aligning the external field  $B_{\rm ext}$  to another NV spin axis, e.g. NV<sub>2</sub> shown in Fig. 1(c), the measured stray field pattern rotates by 90 degrees in the sample plane accordingly [Fig. 3(b)]. It is worth mentioning that NV wide-field imaging of another YIG microdisk with a larger diameter of 16  $\mu$ m also shows the similar experimental features [Fig. 3(c)] regardless of the fact that the measured stray field in the central area of the disk is smaller than that measured for the 10- $\mu$ m-sized sample due to the reduced edge effect. Again, the presented NV wide-field experimental data is supported by micromagnetic simulation results presented in Figs. 3(e) and 3(f).

Lastly, we use wide-field magnetometry techniques<sup>12–15</sup> to investigate the spatially varying NV Rabi oscillations in response to the local stray field arising from the YIG disk. Figure 4(a) shows a 2D map of the measured NV ESR frequency  $f_-$  over the YIG pattern. An external magnetic field  $B_{\rm ext}$  of 400 G is applied along the NV<sub>1</sub> spin axis for the measurements. The emanating magnetic stray field modifies  $f_-$  accordingly following the equation:  $f_- = 2.87 - \gamma$   $B_{\rm NV_1}$ . One can see that the measured NV ESR frequency map shows fragmented areas, consistent with the stray field map shown in Fig. 3(a). Due to the significant spatial variations of  $f_-$ , NV Rabi oscillations can only be locally excited in individual sample areas as shown in Figs. 4(b)-4(d). We

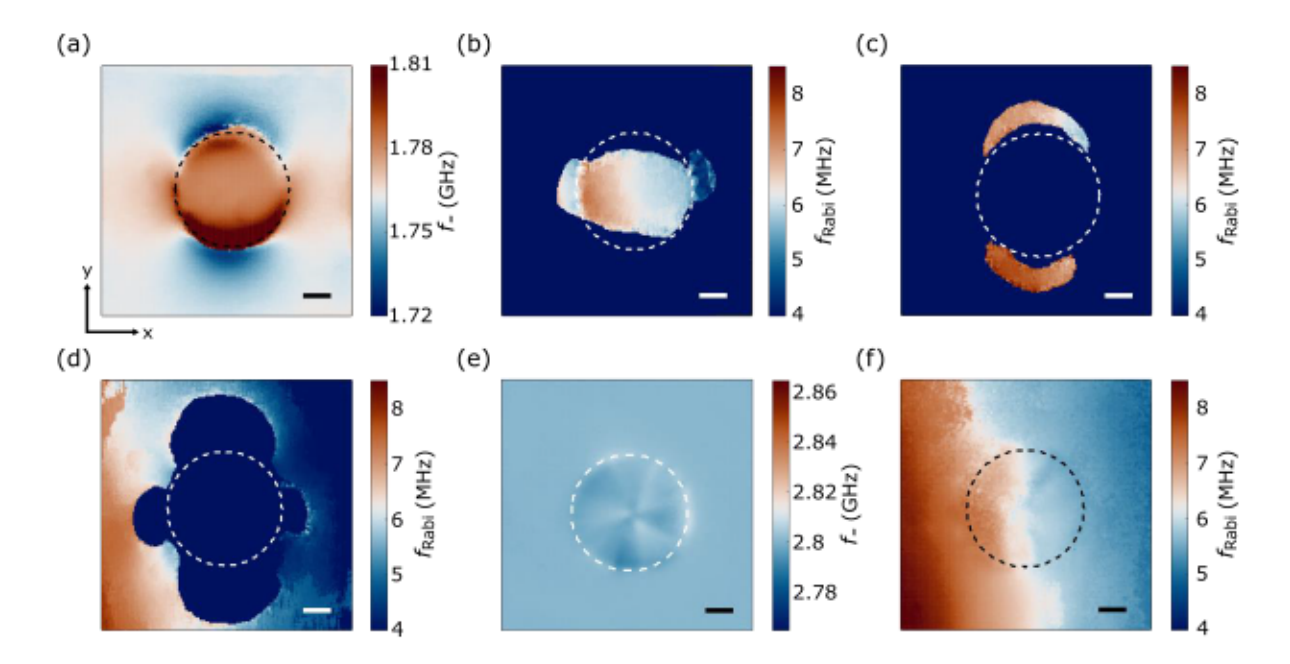


Figure 4. (a) Wide-field imaging of spatially dependent NV ESR frequency  $f_{-}$  in response to local variations of stray field arising from a YIG disk. The YIG magnetization is uniformly aligned in the sample plane by an external magnetic field  $B_{\rm ext} = 400$  G applied along the spin axis of NV<sub>1</sub>. (b)-(d) NV Rabi oscillations locally excited in individual diamond areas at NV ESR frequencies of 1.778 GHz, 1.721 GHz, and 1.758 GHz, respectively. (e) Wide-field imaging of the minor spatial variations of NV ESR frequency  $f_{-}$  in response to stray fields arising from a randomly magnetically polarized YIG disk. (f) NV Rabi oscillations excited over the entire sample areas at a single NV ESR frequency  $f_{-}$ . The black (white) dashed lines outline the boundary of the YIG disk and scale bar is 2.5  $\mu$ m.

also performed control experiments by applying a small out-of-plane magnetic field of  $\sim 25$  G for wide-field NV measurements. Due to the large magnetic anisotropy and vanishingly small in-plane projection of the external magnetic field, the YIG magnetization stays in the disk plane, but exhibits a random distribution without a preferable magnetic orientation. The unsaturated magnetic state naturally results in significantly reduced stray fields emanating from the YIG disk and minor spatial variations of the NV ESR frequency  $f_-$  as shown in Fig. 4(e). Under these conditions, Rabi oscillations can be collectively excited over the entire NV region as shown in Fig. 4(f), and the variation of the NV Rabi frequency results from the spatially varying microwave magnetic fields generated by the on-chip Au stripline. Here it is worth mentioning that the applied NV ESR frequency  $f_-$  is detuned from YIG spin wave frequency  $f_-$  sw for the NV Rabi measurements presented in Fig. 4. When  $f_- = f_{SW}$ , it would be interesting to explore the possibility of direct visualization of YIG spin wave mode profiles using NV ensembles. We reserve this exciting work for future studies.

In summary, we have demonstrated quantum sensing of spin wave modes and magnetic stray fields arising from patterned YIG microdisks. By performing NV ESR and Rabi oscillation measurements using wide-field magnetometry, we achieved direct imaging of the local field environment of YIG patterns at the submicron length scale. The presented experimental data is supported by theoretical predictions and micromagnetic simulation results, demonstrating the reliability and excellent sensitivity of NV quantum metrology techniques. Our work further highlights the significant opportunities of NV spin sensors for probing the local magnetic behaviors in functional magnetic devices, aiding the development of next-generation, high-density, scalable spintronic technologies. 32,33

Supplementary material: See the supplementary material for experimental methods of NV measurements.

Acknowledgements. J. Z., G. Q. Y., and C. R. D. acknowledged the support from U. S. National Science Foundation (NSF) under award No. ECCS-2029558 and No. DMR-2046227. N. J. M., M. H., H. L. W., and C. R. D. were supported by the Air Force Office of Scientific Research under award FA9550-20-1-0319 and its Young Investigator Program under award FA9550-21-1-0125.

## References:

- <sup>1</sup> A. Hirohata, K. Yamada, Y. Nakatani, L. Prejbeanu, B. Diény, P. Pirro, and B. Hillebrands, J. Magn. Magn. Mater. **509**, 166711 (2020).
- <sup>2</sup> M. Julliere, Phys. Lett. A 54, 225 (1975).
- <sup>3</sup> T. Miyazaki and N. Tezuka, J. Magn. Magn. Mater. 139, L231 (1995).
- <sup>4</sup> J. S. Moodera, L.R. Kinder, T.M. Wong, and R. Meservey, Phys. Rev. Lett. 74, 3273 (1995).
- <sup>5</sup> J. G. Zhu, Y. Zheng, and G.A. Prinz, J. Appl. Phys. 87, 6668 (2000).
- <sup>6</sup> D. Apalkov, B. Dieny, and J.M. Slaughter, Proc. IEEE 104, 1796 (2016).
- <sup>7</sup> L. Liu, C.F. Pai, Y. Li, H.W. Tseng, D.C. Ralph, and R.A. Buhrman, Science 336, 555 (2012).
- <sup>8</sup> Q. Shao, P. Li, L. Liu, H. Yang, S. Fukami, A. Razavi, H. Wu, K. Wang, F. Freimuth, Y. Mokrousov, M.D. Stiles, S. Emori, A. Hoffmann, J. Akerman, K. Roy, J.P. Wang, S.H. Yang, K. Garello, and W. Zhang, IEEE Trans. Magn. 57, (2021).
- <sup>9</sup> C. L. Degen, F. Reinhard, and P. Cappellaro, Rev. Mod. Phys. 89, 035002 (2017).
- <sup>10</sup>J. R. Maze, P.L. Stanwix, J.S. Hodges, S. Hong, J.M. Taylor, P. Cappellaro, L. Jiang, M.V.G. Dutt, E. Togan, A.S. Zibrov, A. Yacoby, R.L. Walsworth, and M.D. Lukin, Nature 455, 644 (2008).
- <sup>11</sup> C. Du, T. van der Sar, T.X. Zhou, P. Upadhyaya, F. Casola, H. Zhang, M.C. Onbasli, C.A. Ross, R.L. Walsworth, Y. Tserkovnyak, and A. Yacoby, Science 357, 195 (2017).
- <sup>12</sup> N.J. Mclaughlin, C. Hu, M. Huang, S. Zhang, H. Lu, G.Q. Yan, H. Wang, Y. Tserkovnyak, N. Ni, and C.R. Du, Nano Lett. 22, 5810 (2022).
- <sup>13</sup> T. Lenz, G. Chatzidrosos, Z. Wang, L. Bougas, Y. Dumeige, A. Wickenbrock, N. Kerber, J. Zázvorka, F. Kammerbauer, M. Kläui, Z. Kazi, K.M.C. Fu, K.M. Itoh, H. Watanabe, and D. Budker, Phys. Rev. Appl. 15, 024040 (2021).
- <sup>14</sup> J.P. Tetienne, N. Dontschuk, D.A. Broadway, A. Stacey, D.A. Simpson, and L.C.L. Hollenberg, Sci. Adv. 3, (2017).
- <sup>15</sup> M.J.H. Ku, T.X. Zhou, Q. Li, Y.J. Shin, J.K. Shi, C. Burch, L.E. Anderson, A.T. Pierce, Y. Xie, A. Hamo, U. Vool, H. Zhang, F. Casola, T. Taniguchi, K. Watanabe, M.M. Fogler, P. Kim, A. Yacoby, and R.L. Walsworth, Nature 583, 537 (2020).
- <sup>16</sup> M.W. Doherty, N.B. Manson, P. Delaney, F. Jelezko, J. Wrachtrup, and L.C.L. Hollenberg, Phys. Rep. 528, 1 (2013).
- <sup>17</sup> S.O. Demokritov, V.E. Demidov, O. Dzyapko, G.A. Melkov, A.A. Serga, B. Hillebrands, and A.N. Slavin, Nature **443**, 430 (2006).
- <sup>18</sup> K. An, K.S. Olsson, A. Weathers, S. Sullivan, X. Chen, X. Li, L.G. Marshall, X. Ma, N. Klimovich, J. Zhou, L. Shi, and X. Li, Phys. Rev. Lett. 117, 107202 (2016).
- <sup>19</sup> G. Kucsko, P.C. Maurer, N.Y. Yao, M. Kubo, H.J. Noh, P.K. Lo, H. Park, and M.D. Lukin, Nature 500, 54 (2013).
- <sup>20</sup> L. Thiel, Z. Wang, M.A. Tschudin, D. Rohner, I. Gutiérrez-Lezama, N. Ubrig, M. Gibertini, E. Giannini, A.F. Morpurgo, and P. Maletinsky, Science 364, 973 (2019).
- <sup>21</sup> A. Finco, A. Haykal, R. Tanos, F. Fabre, S. Chouaieb, W. Akhtar, I. Robert-Philip, W. Legrand, F. Ajejas, K. Bouzehouane, N. Reyren, T. Devolder, J.P. Adam, J. von Kim, V. Cros, and V. Jacques, Nat. Commun. 12, 1 (2021).
- <sup>22</sup> R. Ebadi, M.C. Marshall, D.F. Phillips, J. Cremer, T. Zhou, M. Titze, P. Kehayias, M.S. Ziabari, N. Delegan, S. Rajendran, A.O. Sushkov, F.J. Heremans, E.S. Bielejec, M. v. Holt, and R.L. Walsworth, AVS Quantum Sci. 4, 044701 (2022).

- <sup>23</sup> Y. Schlussel, T. Lenz, D. Rohner, Y. Bar-Haim, L. Bougas, D. Groswasser, M. Kieschnick, E. Rozenberg, L. Thiel, A. Waxman, J. Meijer, P. Maletinsky, D. Budker, and R. Folman, Phys. Rev. Appl. 10, 034032 (2018).
- <sup>24</sup> T.I. Andersen, B.L. Dwyer, J.D. Sanchez-Yamagishi, J.F. Rodriguez-Nieva, K. Agarwal, K. Watanabe, T. Taniguchi, E.A. Demler, P. Kim, H. Park, and M.D. Lukin, Science 364, 154 (2019).
- <sup>25</sup> S. Kolkowitz, A. Safira, A.A. High, R.C. Devlin, S. Choi, Q.P. Unterreithmeier, D. Patterson, A.S. Zibrov, V.E. Manucharyan, H. Park, and M.D. Lukin, Science 347, 1129 (2015).
- <sup>26</sup> B.A. McCullian, A.M. Thabt, B.A. Gray, A.L. Melendez, M.S. Wolf, V.L. Safonov, D. v. Pelekhov, V.P. Bhallamudi, M.R. Page, and P.C. Hammel, Nat. Commun. 11, 1 (2020).
- <sup>27</sup> F. Jelezko, T. Gaebel, I. Popa, A. Gruber, and J. Wrachtrup, Phys. Rev. Lett. 92, (2004).
- <sup>28</sup> P. Andrich, C.F. de las Casas, X. Liu, H.L. Bretscher, J.R. Berman, F.J. Heremans, P.F. Nealey, and D.D. Awschalom, NPJ Quantum Inf. 3, 1 (2017).
- <sup>29</sup> E.R.J. Edwards, M. Buchmeier, V.E. Demidov, and S.O. Demokritov, J. Appl. Phys. 113, 103901 (2013).
- <sup>30</sup> Z. Zhang, M. Vogel, J. Holanda, J. Ding, M.B. Jungfleisch, Y. Li, J.E. Pearson, R. Divan, W. Zhang, A. Hoffmann, Y. Nie, and V. Novosad, Phys. Rev. B 100, 014429 (2019).
- <sup>31</sup> H. Yu, O. D'Allivy Kelly, V. Cros, R. Bernard, P. Bortolotti, A. Anane, F. Brandl, R. Huber, I. Stasinopoulos, and D. Grundler, Sci. Rep. 4, (2014).
- <sup>32</sup> D.D. Awschalom, C.R. Du, R. He, F. Joseph Heremans, A. Hoffmann, J. Hou, H. Kurebayashi, Y. Li, L. Liu, V. Novosad, J. Sklenar, S.E. Sullivan, D. Sun, H. Tang, V. Tyberkevych, C. Trevillian, A.W. Tsen, L.R. Weiss, W. Zhang, X. Zhang, L. Zhao, and C.H.W. Zollitsch, IEEE Trans. Quantum Eng. 2, 1-36 (2021).
- <sup>33</sup> D.R. Candido, G.D. Fuchs, E. Johnston-Halperin, and M.E. Flatté, Mater. Quantum Technol. 1, 011001 (2020).